RESEARCH ARTICLE

Correspondence to:
A. Doré,
arnaud.dore@u-bordeaux.fr

Numerical modeling of subaqueous sand dune morphodynamics

Arnaud Doré[1], Philippe Bonneton[1], Vincent Marieu[1], and Thierry Garlan[2]

[1]Université de Bordeaux, CNRS, UMR, Talence, France, [2]SHOM, HOM/REC-CFuD/Sédimentologie, Brest, France

Abstract The morphodynamic evolution of subaqueous sand dunes is investigated, using a 2-D Reynolds-averaged Navier-Stokes numerical model. A laboratory experiment where dunes are generated under stationary unidirectional flow conditions is used as a reference case. The model reproduces the evolution of the erodible bed until a state of equilibrium is reached. In particular, the simulation exhibits the different stages of the bed evolution, e.g., the incipient ripple generation, the nonlinear bed form growing phase, and the dune field equilibrium phase. The results show good agreement in terms of dune geometrical dimensions and time to equilibrium. After the emergence of the first ripple field, the bed growth is driven by cascading merging sequences between bed forms of different heights. A sequence extracted from the simulation shows how the downstream bed form is first eroded before merging with the upstream bed form. Superimposed bed forms emerge on the dune stoss sides during the simulation. An analysis of the results shows that they emerge downstream of a slight deflection on the dune profile. The deflection arises due to a modification of the sediment flux gradient consecutive to a reduction in the turbulence relaxation length while the upstream bed form height decreases. As they migrate, superimposed bed forms grow on the dune stoss side and eventually provoke the degeneration of the dune crest. Cascading merging sequences and superimposed bed forms dynamics both influence the dune field evolution and size and therefore play a fundamental role in the dune field self-organization process.

1. Introduction

Sand dunes are ubiquitous bed forms in nature within subaqueous environments. Sand dunes interact with the flow in a retroactive way, generating a complex turbulent flow downstream of the crests [*Nelson et al.*, 1993; *Bennett and Best*, 1995; *Venditti*, 2007] and complex near bed sediment processes along the migrating dunes profiles [*Naqshband et al.*, 2014, 2015]. This leads to an increase of the flow resistance [*Engelund*, 1966; *Fredsøe and Deigaard*, 1992]. Understanding dune evolution is therefore an important issue to accurately predict the flow circulation, the sediment fluxes, and the bathymetric variations in sandy subaqueous environments. Sand dunes may pose a significant risk for offshore activities in coastal environments, especially with the growing development of renewable marine energy [*Todd et al.*, 2014; *Barrie and Conway*, 2014]. Also, linking the characteristics of cross-stratification data with the flow that created them is potentially a powerful tool for paleoenvironmental reconstruction of ancient flow conditions [*Leclair*, 2002; *Reesink and Bridge*, 2007]. Although sand dunes represent a great scientific and operational interest, their evolution is still poorly understood due to their complex behavior.

Observations of bed form development under various flow conditions show that an initially flat bed evolves through different phases, an incipient bed form phase, a growing bed form phase, and a stabilizing phase leading to a fully developed dune field [*Baas*, 1994, 1999; *Perillo et al.*, 2014]. In the first stages of the bed evolution, the initially flat erodible sand bed sheared by a stationary flow is unstable when the threshold of sediment motion is exceeded somewhere on the domain. Small perturbations arise either sparsely as random pileups for shear velocities close to the threshold or spontaneously all over the bed for higher shear velocities, organizing into straight crest lines [*Venditti et al.*, 2005a]. These first perturbations grow exponentially with time until a homogeneous ripple field is formed [*Betat*, 1999; *Fourrière et al.*, 2010]. During this phase the incipient ripple wavelength remains constant and is linked to the roughness of the bed, scaling whether on the viscous length or on the grain size, depending on the shear velocity [*Valance and Langlois*, 2005; *Valance*, 2005; *Charru*, 2006]. Many laboratory and field experiments allowed for the observation of the initial ripples development, revealing wavelengths of the order of a few centimeters (of the order $O(10^2)d_{50}$ to $O(10^3)d_{50}$)

and development time scales of a few tens of seconds [*Yalin*, 1985; *Coleman and Melville*, 1996; *Baas*, 1999; *Betat*, 1999; *Langlois and Valance*, 2007; *Fourrière et al.*, 2010].

The instability of an erodible bed during this incipient phase has been studied theoretically for many years through the mathematical analysis of bed response to small perturbations. They revealed that the instability mechanism is due to a phase shift between the bed and the shear stress enhanced by the bed friction [*Kennedy*, 1963; *Engelund*, 1970; *Richards*, 1980; *McLean*, 1990; *Colombini*, 2004]. The analysis was further extended for smooth flow conditions [*Sumer and Bakioglu*, 1984; *Charru and Mouilleron-Arnould*, 2002]. *Colombini and Stocchino* [2011] proposed a linear stability analysis for dune and ripple formation valid in the smooth as well as in the transitional and rough flow regimes. The cutoff wave number and the most unstable mode were found to be sensitive to both the effect of gravity on an inclined slope [*Fredsøe*, 1974] and the sediment flux inertia [*Charru and Mouilleron-Arnould*, 2002; *Valance and Langlois*, 2005; *Valance*, 2005; *Charru and Hinch*, 2006].

Beyond the incipient ripple generation phase, the bed evolution becomes highly nonlinear. The small perturbation hypothesis no longer holds as soon as the ratio of the bed wave amplitude, η, to the wavelength, λ, exceeds a threshold value, $2\eta/\lambda \simeq 0.03$, then the hydrodynamical nonlinear effects are no longer negligible [*Charru et al.*, 2013]. Slight differences in ripple heights lead to different migration velocities, as initially shown by *Bagnold* [1941] for the aeolian case. As a consequence, bed forms interact in cascading merging sequences until a homogeneous steady migrating dunes field is eventually obtained [*Mantz*, 1978; *Baas*, 1994; *Coleman and Melville*, 1994; *Betat et al.*, 2002; *Coleman et al.*, 2003; *Venditti et al.*, 2005a]. *Best et al.* [2013] observed experimentally this "amalgamation process" between two bed forms, in a narrow flume, and revealed the importance of the interactions between the flow separation zones, the flow sheltering, and the leeside erosion. The final dune wavelengths scale on the water depth as shown, for instance, in the extensive flume data of *Guy et al.* [1966] for a broad range of sand diameters and representative flow conditions. Equilibrium wavelengths ranged between D_0 and $30D_0$ in the experimentations, with D_0 as the water depth. Classifications based on geometrical considerations are usually employed to distinguish ripples and dunes [*Boothroyd and Hubbard*, 1975; *Dalrymple et al.*, 1978; *Ashley*, 1990], which lead to heterogeneous terminologies. Moreover, geometrical criteria are questionable, especially when there is no clear separation of length scale between the spacing of ripple crests and the flow depth. A classification based on the physical mechanisms that influence bed form dynamics is therefore preferable. Dune growth is limited by the water depth, through a gradual decrease in the phase shift of the bed shear stress τ_b, and as such their dynamics is distinct from that of ripples [*Fourrière et al.*, 2010; *Charru et al.*, 2013]. Ripples can be defined as bed forms whose size is too small compared to the water depth to interact with the free surface. *Fourrière et al.* [2010] demonstrated that for modes scaling on the water depth, $KD_0 \simeq O(1)$, with K the wave number; wavelengths are stabilized by the presence of the free surface through a resonant condition which depends on the Froude number. Experimental evidence also suggests that dunes rather emerge from the pattern coarsening of ripples rather than by linear instability [*Charru et al.*, 2013]. Figure 1 shows some experimental data represented in a (KD_0, Fr) diagram. The resonant value is represented by a line that separates the ripples in the supercritical region, wave number larger than the resonant value, and dunes in the subcritical region, wave number smaller than the resonant value and which are affected by the presence of the free surface [*Fourrière et al.*, 2010; *Charru et al.*, 2013]. It is worth noting that in this diagram the flume data set of *Guy et al.* [1966] lie in the dune region.

Observations have shown that superimposed bed forms can appear on the stoss side of dunes once they reached a reasonable size, emerging at a variable distance between the reattachment point and the dune crest [*Venditti et al.*, 2005b; *Jerolmack and Mohrig*, 2005; *Martin and Jerolmack*, 2013; *Warmink et al.*, 2014]. Their generation mechanisms are still unknown and interactions between dunes and superimposed bed forms are poorly understood. According to *Reesink and Bridge* [2009], superimposed bed forms reaching a threshold height start to erode the principal dune profile. These bed forms could be linked to the dune splitting process [*Warmink et al.*, 2014].

Knowledge of the physical processes driving the bed evolution has mainly been gathered through experimental studies in the past. Thanks to constantly increased computer capabilities, during the last decade, numerical modeling allowed for a further description of the nonlinear dynamics driving the bed development beyond the incipient ripple generation phase. Numerical modeling enables the simultaneous resolution and the study of the links between flow structure, sediment transport, and the evolving bed topography [*Best*, 2005]. Two dimensional approaches have successfully been employed to reproduce the growth of the bed form field.
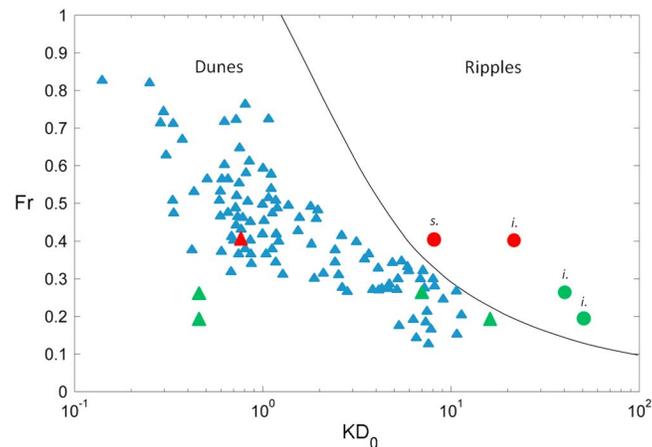
Figure 1. Data set of bed forms in the plane (KD_0,Fr) from flume experiments and measurements in nature. Blue symbols: flume experiments of *Guy et al.* [1966]. Green symbols: experiments in nature of *Fourrière et al.* [2010]. Red symbols: simulation of the flume experiment EXP1 of *Naqshband et al.* [2014]. The black line represents the resonant curve separating dunes from ripples. The dots represent the incipient (i.) and superimposed (s.) ripples, and the triangles represent the dunes at equilibrium. Figure modified from *Fourrière et al.* [2010].

For example, *Giri and Shimizu* [2006] realistically replicated some key physical features during the bed form evolution, such as bed form merging or the asymmetric nature of the dune shapes. They used a Reynolds-averaged Navier-Stokes (RANS) model with a pickup and deposition formulation for the sediment transport; however, the latter induced an artificial redistribution of the sediment and the bed form could not reach an equilibrium state. *Niemann* [2011] showed that the equilibrium dune profile shape for a given wavelength is essentially determined by the magnitude of the Shields number on the plane bed, obtaining results in line with *Tjerry and Fredsøe* [2005]. They also pointed out the role of the relaxation of the turbulence and the bed curvature in setting up the dune dimensions. *Tjerry and Fredsøe* [2005] improved the semiempirical approach of *Fredsøe* [1982] with a description of the flow including a turbulence k-ϵ formulation. The flow description allowed for the calculation of more realistic sand dune geometry at equilibrium which compared fairly well to various field data. However, this model calculates dune shapes with a fixed height and therefore cannot be used to simulate the bed morphodynamic evolution from the quasi-flat bed. *Paarlberg et al.* [2009], by adding a parameterization of the flow separation zone in a hydrostatic model, showed the significant role of the separation zone both in the final dune shape and on the time to equilibrium. This parametric approach is attractive due to the low computation time to resolve the hydrodynamic field. However, this method cannot resolve dune saturation. *Warmink et al.* [2014] extended the model of *Paarlberg et al.* [2009] with a parameterization of superimposed bed forms. Making the assumption that superimposed bed forms control the saturation of the dune field, the authors artificially introduced superimposed bed forms on the stoss side of the dunes to provoke dune splitting. The superimposed bed form wavelengths scale on the water depth and correspond to dunes; therefore, the model simulates merging sequences rather than dune splitting. Moreover, it is unlikely that superimposed bed forms are responsible for the saturation, as in various experimentations, the sand dune field reach the equilibrium without superimposed bed forms on dunes stoss side [*Coleman and Melville*, 1994; *Fourrière et al.*, 2010; *Naqshband et al.*, 2014]. Recently, *Nabi et al.* [2013], by using a large eddy simulation model coupled with a sediment pickup and deposition Lagrangian formulation were able to reproduce the evolution of 3-D dunes. The spanwise sediment transport is reproduced by the inclusion of a turbulent step length within a sediment pickup model. During the simulations the turbulent shear stress fluctuations on sediment pickup trigger the generation of superimposed bed forms.

Numerical modeling studies usually do not reproduce the first stage of evolution of a quasi-flat bed leading to the generation of incipient ripples. Merging between bed forms are observed in experiments, but little is known about the different steps of a merging sequence and the physics involved. Superimposed bed forms are frequently observed on dune profiles, but their formation mechanisms and the way they interact with the larger dunes are still under debate.

In the present work we reproduce the different steps of the morphodynamic evolution of an erodible bed, made up of noncohesive sediments, under steady unidirectional conditions, by using a 2-D RANS approach.
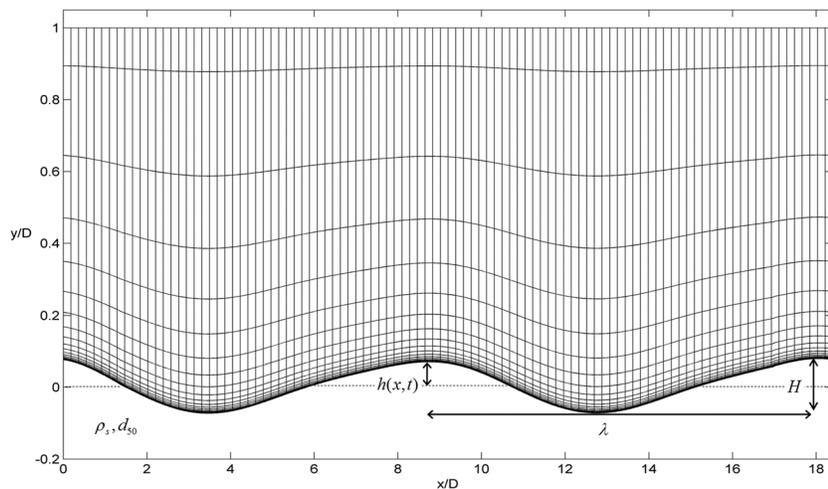
Figure 2. Computational grid used over two dunes in the simulation (800 × 40). One of four grid cells is plotted in the *x* direction.

In the next section, we present the model, the different modules it encompasses, and its calibration. In section 3 we present the scenario that is simulated in section 4, where we reproduce both the incipient ripple generation phase and the nonlinear growing phase until saturation is reached.

2. Numerical Model Description

The numerical model used herein is an evolved version of DUNE2D initially developed by *Tjerry* [1995] at the Danish Technical University to perform morphological calculations of sand dunes. The model was previously used by several authors under different versions to study sand dunes shapes under stationary currents [*Niemann*, 2003; *Tjerry and Fredsøe*, 2005] or the morphodynamic evolution of wave-generated orbital ripples [*Andersen*, 1999; *Marieu et al.*, 2008].

The flow model allows for a good description of the boundary layer over the dune profile and of the lag effect between the bed profile and the flow, which is crucial in dunes morphological evolution. The model describes the nonhydrostatic pressure field and therefore reproduces the separation behind dune crests. The flow equations are solved by means of a finite volume method with an ISNAS scheme [*Zijlema*, 1996], on a curvilinear orthogonal grid, which allows the grid to adjust to the bed evolution (Figure 2).

The grid is generated by the transfinite interpolation method of *Eriksson* [1982], after each morphological calculation. The size of the closest cell to the bed is chosen in order to properly resolve the viscous sublayer. For the studied configurations the Froude number remains low ($Fr \simeq 0.4$), which insures that the effect of the deformation of the free surface is negligible [*Fredsøe*, 1982], and allows for a rigid lid condition at the free surface, where the vertical velocity is zero. Periodic conditions are applied to the left and the right sides of the domain. At the bed a no-slip boundary condition is used with zero horizontal and vertical velocities. In this study, the bed is composed of quartz sand of relative density $s = \frac{\rho_s}{\rho} = 1.65$, ρ and ρ_s, respectively, being the fluid and sediment density. The sediment median grain diameter is d_{50}, λ and H are, respectively, dunes wavelength and height (Figure 2).

The model includes three modules: the hydrodynamic module solves the flow equations and the turbulence field, the sediment transport module computes the bed load and the suspended load transport, and the morphological module solves the bed evolution equation. A more in-depth description of the three modules is given in the following. Further explanations about the numerical methods of resolution are available in *Tjerry* [1995].

2.1. Hydrodynamic Model
The flow model solves the RANS equations and the equation of mass conservation:

$$\frac{\partial U_i}{\partial t} + U_j \frac{\partial U_i}{\partial x_j} = -\frac{1}{\rho}\frac{\partial P}{\partial x_i} + \frac{\partial}{\partial x_j}\left(2\nu S_{ij} + \tau_{ij}\right) \tag{1}$$

$$\frac{\partial U_i}{\partial x_i} = 0, \tag{2}$$

where U_i are the averaged fluid velocity components, $i = 1, 2$ representing x and y, the horizontal and vertical coordinates. P is the pressure, ρ the water density, ν the dynamic viscosity, and S_{ij} the strain rate tensor $S_{ij} = \frac{1}{2}\left(\frac{\partial U_i}{\partial x_j} + \frac{\partial U_j}{\partial x_i}\right)$.

The Reynolds stress tensor, τ_{ij}, is obtained using a k-ω model, with k the kinetic energy and ω, the specific dissipation:

$$\tau_{ij} = 2\nu_T S_{ij} - \frac{2}{3}k\delta_{ij}, \tag{3}$$

where the eddy viscosity, $\nu_t = \gamma^* \frac{k}{\omega}$, is directly obtained from k and ω from the resolution of the closure equations:

$$\frac{\partial k}{\partial t} + U_j \frac{\partial k}{\partial x_j} = \frac{\partial}{\partial x_j}\left[(\nu + \sigma^* \nu_T)\frac{\partial k}{\partial x_j}\right] - \overline{u_i u_j}\frac{\partial U_i}{\partial x_j} - \beta^* k\omega$$

$$\frac{\partial \omega}{\partial t} + U_j \frac{\partial \omega}{\partial x_j} = \frac{\partial}{\partial x_j}\left[(\nu + \sigma \nu_T)\frac{\partial \omega}{\partial x_j}\right] + \gamma \frac{\omega}{k}\left(-\overline{u_i u_j}\frac{\partial U_i}{\partial x_j}\right) - \beta\omega^2,$$

where β, β^*, σ, σ^*, and γ are closure coefficients. The two-equation k-ω closure model insures a good description of the flow recirculation in the leeside of the bed forms [*Andersen*, 1999].

A Pressure Implicit Splitting Operators algorithm is employed for the resolution of the governing equations following the approach of *Patankar* [1980]. The mean current is obtained by iteration on an additional volume force in the momentum equations, using a proportional integral derivative (PID) control algorithm set by *Andersen* [1999]. The PID control algorithm calculates an error value between the calculated and the desired flux. The volume force is specified explicitly in function of the error value and relaxation factors. The procedure is repeated until the desired flux is obtained.

2.2. Sediment Transport Model

The model computes separately the near-bed transport (bed load fraction) and the transport integrated along the water column (suspended load fraction). The bed load transport, q_b, is calculated with the formula given by [*Meyer-Peter and Müller*, 1948]:

$$\begin{cases} q_b(x,t) = 8\left(\theta(x,t) - \theta_{c\alpha}(x)\right)^{\frac{3}{2}} & \text{if } \theta(x,t) > \theta_{c\alpha}(x) \\ q_b(x,t) = 0 & \text{if } \theta(x,t) \le \theta_{c\alpha}(x) \end{cases} \tag{4}$$

where θ is the Shields number and $\theta_{c\alpha}$ is the slope corrected critical Shields number [*Fredsøe and Deigaard*, 1992]. The suspended sediment concentration, c, is calculated through the resolution of the advection-diffusion equation:

$$\frac{\partial c}{\partial t} + u_j \frac{\partial c}{\partial x_j} = \frac{\partial w_s c}{\partial z} + \frac{\partial}{\partial x_j}\left(\nu_T \frac{\partial c}{\partial x_j}\right), \tag{5}$$

where w_s is the settling velocity defined by

$$w_s = \sqrt{\frac{4(s-1)gd_{50}}{3C_D}}, \tag{6}$$

C_D being the drag coefficient for natural sand, d_{50} the median grain diameter, and s is the relative grain density, with a value of $s = 2.65$ for quartz-dominated natural sediments [*Fredsøe and Deigaard*, 1992].

The bed concentration c_b is determined at the height $y = h + 2d_{50}$, where h is the bed height, according to *Engelund and Fredsøe* [1976]. The suspended sediment transport is found by integration of the suspended concentration flux over the water column:

$$q_s(x, t) = \int_{h(x,t)}^{D_0} c(x, y, t) u(x, y, t) \, dy, \tag{7}$$

D_0 being the elevation of top water rigid boundary.

2.3. Morphological Model

The bed evolution is solved through the sediment conservation equation

$$\frac{\partial h}{\partial t} + \frac{\partial q}{\partial x} = 0 \tag{8}$$

where h is the bed height and q is the total sediment flux given by

$$q = \frac{1}{1 - p} \left(q_b + q_s \right) \tag{9}$$

where p is the porosity of the bed ($p = 0.4$).

The equation is solved using the modified nonoscillatory-centered scheme of *Marieu et al.* [2008] coupled to an avalanche module for the steep lee face of the bed forms. This scheme is able to resolve the high flux peaks at the bed form crests and advantageously replaced the former QUICK scheme used in previous versions of the model [*Niemann*, 2003].

2.4. Decoupling and Numerical Stability

In this study, the hydrodynamics and morphodynamics are solved separately, as the mean current is stationary. The bed morphology is updated once the hydrodynamics has converged to a stationary state, which is justified regarding the small adaptation time of the hydrodynamics compared to the bed evolution. The morphological time step is adapted to the sediment fluxes, in order to avoid spurious oscillations if too large, or bathymetry smoothing due to numerical diffusion if too small. This is performed automatically by monitoring a "morphological Courant number," which is ideally kept below unity:

$$\mathrm{CFL}_{\mathrm{morph}} = a(x) \frac{\Delta_t}{\Delta_x} < 1 \tag{10}$$

where $a(x)$ is the local bed celerity, Δ_t and Δ_x are, respectively, the morphological time step and the spatial step. For a steady migrating bed form, the migration velocity is constant along the profile and $a(x) = \partial q / \partial h$ [*Tjerry and Fredsøe*, 2005; *Niemann*, 2003]. The celerity is approximated in the model at the grid point i, at the time step $n + 1$, and $a_i^{n+1} = \frac{\Delta_x}{\Delta_t} \frac{h_i^{n+1} - h_i^n}{h_{i+\frac{1}{2}}^n - h_{i-\frac{1}{2}}^n}$.

3. Case Study and Model Setup

The modeling scenario is inspired by the experiment EXP1 of *Naqshband et al.* [2014]. The bed evolution was followed up in time in a 30 m long flume, with a narrow width of 0.5 m. The sand was uniform with $d_{50} = 0.29$ mm. The water depth was set to $D_0 = 0.25$ m and the mean velocity to $U = 0.64$ m s^{-1}. The characteristics of the bed forms were monitored along a measuring length of 8 m in the middle section of the flume. The narrow width resulted in a field of quasi 2-D sand dunes. The experimental conditions are represented in the (KD_0, Fr) diagram in Figure 1.

Measurements were carried out using an acoustic concentration and velocity profiler, allowing for the measurement of high-resolution profiles of simultaneous velocity and sediment concentration in the near-bed region and all along the water column. An acoustic interface detection method was employed in order to separate the bed load from the suspended load. After a certain period of time a steady dune field emerged, migrating at a constant speed. During the experiment, superimposed bed forms developed on the stoss side of the dunes and migrated toward the crests.

More information on the experimental set up is available in *Naqshband et al.* [2014].

Table 1. Model Parameters[a]

Parameter	Value
D_0 (m)	0.25
U (m s^{-1})	0.64
k_N (mm)	0.72
ϕ	33°
Δx (m)	0.0057
u^* (m s^{-1})	0.031
w_s (m s^{-1})	0.036

[a]D_0, water depth; U, mean velocity; k_n, bed rugosity; ϕ, angle of repose of the sediment; Δx, Horizontal size of the grid cells; u^*, bed shear velocity; w_s, sediment settling velocity.

3.1. Model Setup

The model is forced with EXP1 setup. The bed roughness is given in terms of the equivalent Nikuradse roughness for a flat bed and $k_N = 2.5d_{50}$ [*Nikuradse*, 1933]. The angle of repose of the sediment is extracted from the figures in *Naqshband et al.* [2014] and is set to $\phi = 33°$, which is in accordance with values found in the literature for immersed sand [*Fredsøe and Deigaard*, 1992; *Van Rijn*, 1993; *Soulsby*, 1997].

The model sensitivity to the mesh resolution has been investigated, and it is found that a minimum number of 35 grid cells per wavelength is necessary for the nonlinear bed form development phase, which is in agreement with previous studies [*Niemann*, 2003; *Marieu et al.*, 2008; *Nabi et al.*, 2013]. This led to N_x=800 grid cells in the horizontal direction in order to cover the $L = 4.6$ m domain length. The vertical resolution must be good enough to resolve the flow in the boundary layer. *Wilcox* [1993] recommended that the lower grid cells (near the bottom) should be smaller than $y = \frac{v}{u^*}$, with u^* the shear velocity, and should use an average near-bed resolution of Δy=0.2$\frac{v}{u^*}$ in his numerical applications for various boundary layer test cases. An even finer resolution is required to resolve the viscous sublayer with our model, and the near-bottom grid cells height is set to $\Delta y = 0.1\frac{v}{u^*}$ here. A good fit between the velocity profile and the theoretical asymptotic values in both the turbulent and the viscous layers for the flat bed case is insured by this mean, and several grid cells are situated in viscous sublayer. Of note, the resolution is higher than in previous applications of the hydrodynamic model, for instance, *Niemann* [2003] used a resolution of $\Delta y = \frac{v}{u^*}$. The grid cells height is increasing geometrically over the water depth, and eventually, the number of grid cells in the vertical direction is kept reasonable, with $N_y = 40$.

Table 1 presents an overview of the parameters used in the simulations presented in this paper.

4. Results

4.1. Evolution From a Quasi-Flat Bed

In the experiment carried out by *Naqshband et al.* [2014], the bed was flattened manually and small perturbations were still present on the initial bed, with $<\lambda> = 0.2$ m and $<H> = 0.2$ m for the mean wavelength and height, respectively, on the monitored section of the flume. The presence of these perturbations prevent the observation of the initial phase of ripple generation, the initial perturbations being larger than incipient ripples. However, the model is able to simulate the incipient ripple generation phase, starting with a quasi-flat bed. Here the initial bed is flat with the presence of randomly distributed small perturbations ($H = O(d_{50})$), which is well below the dimensions of the incipient ripples observed for similar grain sizes [*Coleman and Melville*, 1996; *Raudkivi*, 1997; *Fourrière et al.*, 2010]. In order to shorten significantly the simulation duration, the length of the domain is set to $L = 2.3$ m for this scenario, which is sufficient to end up with several ripples on the domain. The wavelength, λ, and the height, H, of bed forms are retrieved by computing the autocorrelation of the bed profile. This method of analysis enables the relative influence of bed forms of different magnitudes to be correctly evaluated without necessitating any preliminary screening of small bed form data [*Coleman and Melville*, 1994]. The position of the secondary maximum of autocorrelation gives the dominant wavelength on the domain and its amplitude gives the corresponding height.

The result of the temporal bed evolution is presented in Figure 3. The flow direction is oriented from left to right on the figure. This initial phase can be divided in two distinct periods of evolution, for $0 \le t \le 30-40$ s, then for $t > 30-40$ s. From $t = 0$ s to $t \simeq 30-40$ s, the initial perturbations are rapidly growing to heights of about $H/d_{50} \simeq 10-14$, while migrating in the flow direction from the beginning of the evolution. In the simulation results, no recirculation zones are observed in the leeside of the perturbations at this stage of development of the bed. A first conclusion is that the presence of a recirculation zone is not a necessary condition for the migration nor the growth of the perturbations, which is in contrast with previous authors' assumptions in the frame of experimental studies [*Southard*, 1971; *Best*, 1992; *Venditti et al.*, 2005a].
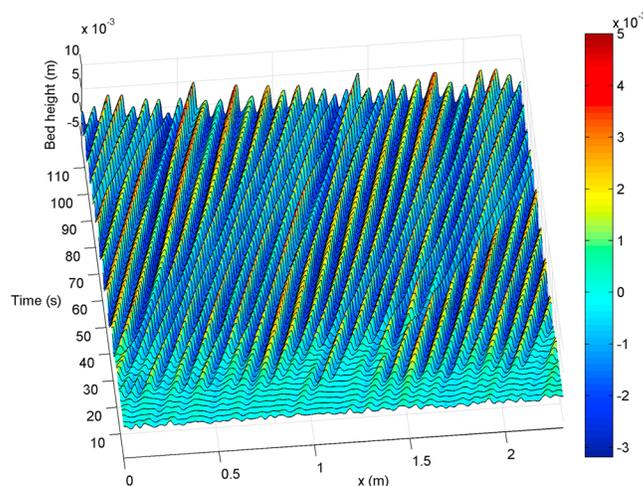
Figure 3. Time evolution of a quasi-flat bed in the early stages between $t = 0$ s and $t = 120$ s.

After $t \simeq 30$–40 s, 33 ripples are already present on the bed. This number is kept constant during the initial phase (see Figure 3). We observed in the simulations that the first recirculation zones are developing at around $t \simeq 30$ s as the ripples start to equilibrate with one another. Ripples height is also adjusting in time leading to a quasi-homogeneous ripple field, of mean height $H/d_{50} \simeq 14$ (Figure 3). The mean height of the ripples and steepness are in agreement with experimental studies with equivalent sand diameters and forcing conditions [*Coleman and Melville*, 1996; *Fourrière et al.*, 2010]. No merging sequences are observed in the simulation until this stage of evolution. The nascent ripples migrate downstream at a velocity of $c \approx 6$ mm s^{-1} and their profiles become asymmetrical and oriented in the flow direction.

The simulation reproduces the behavior of the developing bed in the first stage of its evolution as it has been observed in several experiments [*Coleman and Melville*, 1996; *Betat*, 1999; *Fourrière et al.*, 2010] or demonstrated by mathematical theory [*Valance*, 2005; *Charru*, 2006; *Fourrière et al.*, 2010; *Charru et al.*, 2013]. Both have shown an exponential growth of the bed height and the emergence of ripples with a preferred wavelength. A quantitative analysis of the results shows that the model reproduces this wavelength with good accuracy. Figure 4 shows the time series of the mean height and wavelength of the perturbations. The mean wavelength remains remarkably constant after $t \simeq 15$ s with a value of $\lambda/d_{50} \simeq 240$, which is in agreement with the experiments of *Coleman and Eling* [2000] and *Coleman et al.* [2003], who found a relationship linking the initial stage ripples wavelength and the mean grain diameter, $\lambda = 175 d_{50}^{0.75}$, leading to a value of $\lambda/d_{50} \simeq 238$. Based on experimental data, *Raudkivi* [1997] found $\lambda = 150 d_{50}^{0.5}$, leading to $\lambda/d_{50} \simeq 275$.

The simulation results are also in good agreement with the mathematical models. The most unstable mode is expected to correspond to the observed wavelength emerging from an initially flat bed, at least for the first moments when nonlinear effects are still negligible [*Charru et al.*, 2013]. In their mathematical analysis, *Fourrière et al.* [2010] found a value of $\lambda/L_{sat} \simeq 15$ for a ratio $u^*/u_c = 2.5$, L_{sat} being the saturation length of the sediment transport and u_c being the critical velocity for sediment motion. L_{sat} was determined from several experimental measurements and has a value of $L_{sat} \simeq 15 d_{50}$. For a value of $L_{sat} \simeq 15 d_{50}$, *Charru et al.* [2013] found a ratio of $\lambda/L_{sat} \simeq 15$. Both mathematical studies lead to a wavelength of $\lambda/d_{50} \simeq 225$ in good agreement with the simulated value of $\lambda/d_{50} \simeq 240$.

Figure 4 shows that the bed height experiences an exponential growth until $t \simeq 40$ s and then remains constant with $H/d_{50} = 14$ until the beginning of the nonlinear bed development phase. The bed growth rate can be calculated for the incipient phase and $\sigma = 0.09$ s^{-1}. This is in good agreement with *Charru et al.* [2013] (equation (21)) that would lead to $\sigma = 0.11$ s^{-1}, using the appropriate parameters. It can be concluded that the model accurately reproduces the incipient ripple generation phase from a quasi-flat bed both qualitatively and quantitatively. The position of the incipient ripples ($KD_0 \simeq 22.4$) is shown on the (KD_0, Fr) diagram in Figure 1.

The nonlinear bed development phase was simulated using *Naqshband et al.* [2014] EXP1 experiment conditions and the results are shown in the next section.
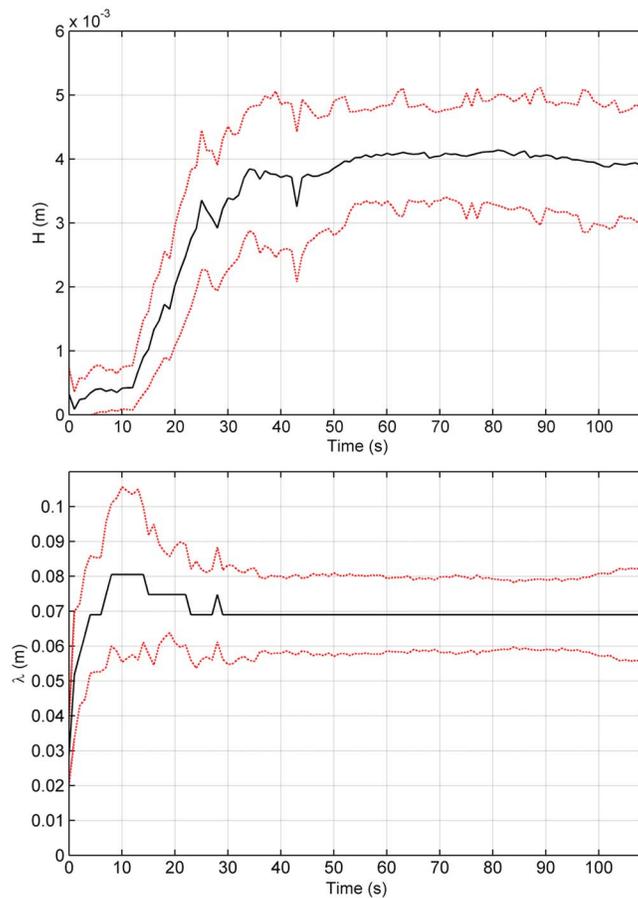
Figure 4. Time series of the evolution of the (top) height and of the (bottom) wavelength of the bed perturbations determined by autocorrelation starting with an initially quasi-flat bed. The dashed red lines represent $H \pm$ std (Figure 4, top) and λ pm std (Figure 4, bottom), with std as the standard deviation.

4.2. Nonlinear Bed Development

In this section, the numerical model is used to reproduce the nonlinear bed development. The bed forms characteristics are retrieved using a method similar to the bed form tracking method of *Van der Mark et al.* [2008] and based on the detection of the zero crossings associated to individual bed forms. The average wavelength and height of the bed forms are given by $<\lambda>=L/n$, n being the number of bed forms detected and
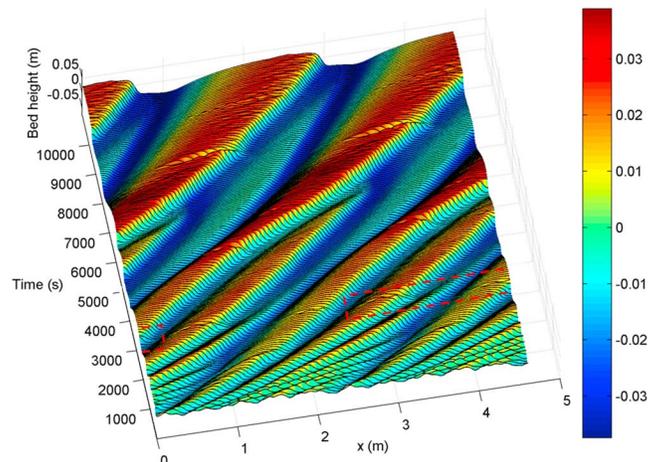

Figure 5. Time evolution of the bed. The initial bed is statistically equivalent to the sandy bottom in *Naqshband et al.* [2014].
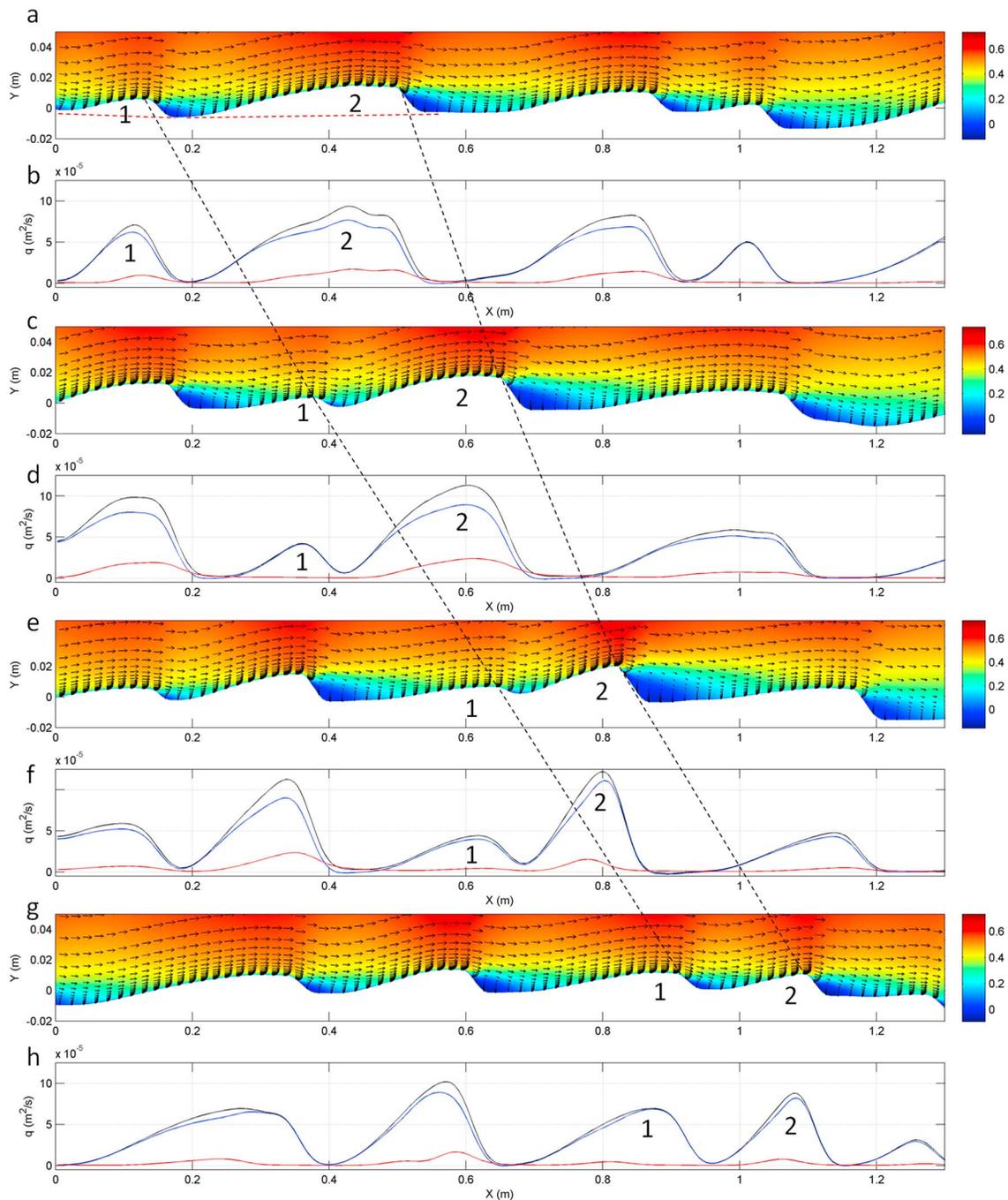
Figure 6. First stage of a merging sequence, with (a, c, e, and g) the velocity field over the bed profile and (b, d, f, and h) the bed load (blue), suspended load (red), and total sediment flux (black) at (b) $t = 100$ s, (d) $t = 200$ s, (f) $t = 300$ s, and (h) $t = 400$ s.

$<H> = \sum_{i=1}^{n} H_i/n$, H_i being the individual bed form heights. The temporal bed evolution starting from the initial bed is shown on Figure 5. In order to take into account the effect of the bed form history, it is necessary to introduce an initial bed topography close to the one used in the experimentation to provide a consistent comparison with EXP1 [*Naqshband et al.*, 2014]. The initial bed is thus set up as a series of random perturbations with $<\lambda>$ = 0.2 m and $<H>$ = 0.02 m.

At the beginning of the simulation, small bed forms migrate faster than the larger ones and eventually merge with the bed forms situated downstream ($0 \leq t \leq 1500$ s), decreasing the number of bed forms (Figure 5). For $t > 1500$ s, as the sand dunes are growing, their migration velocity decreases and the merging sequences
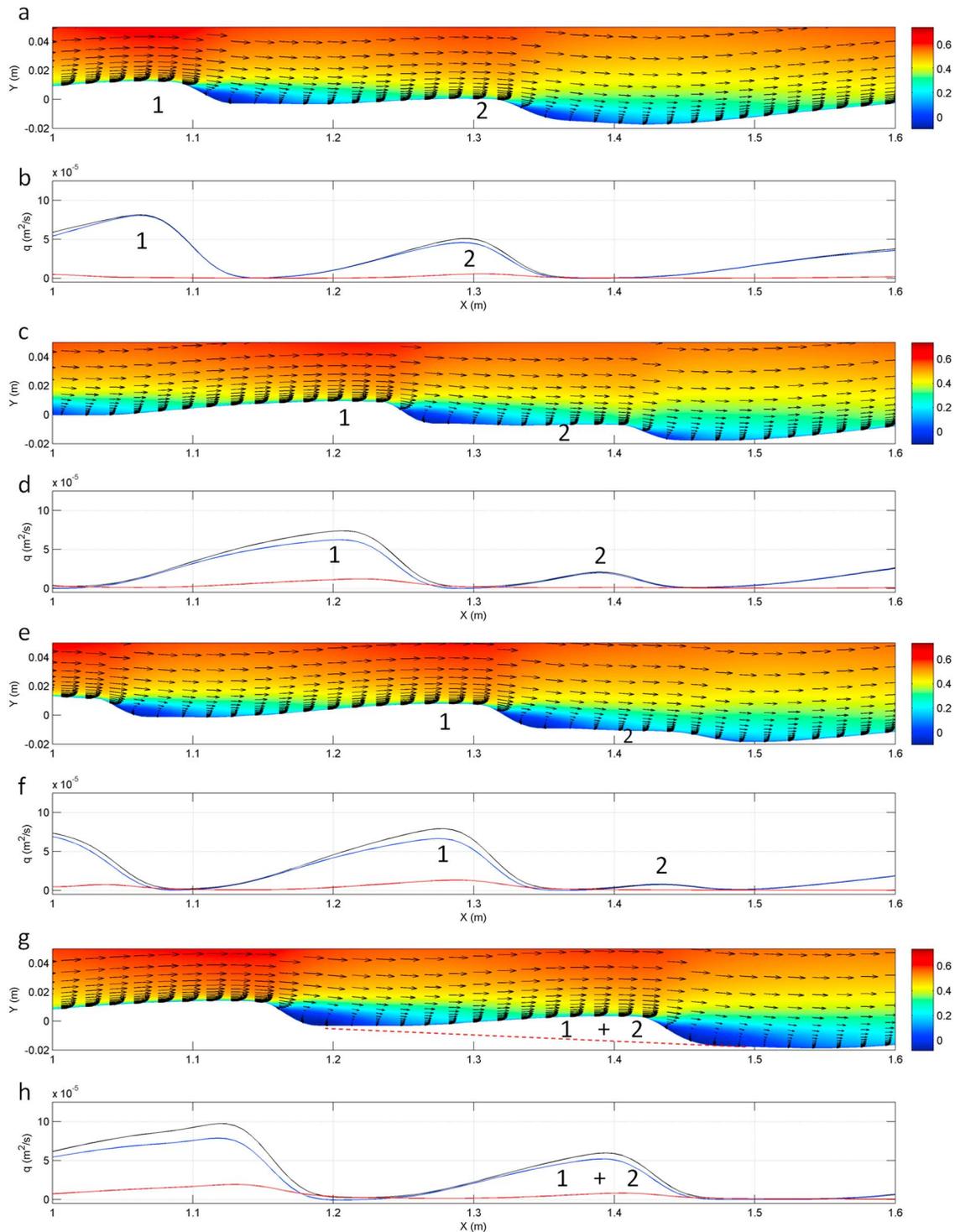
Figure 7. Final stage of a merging sequence, with (a, c, e, and g) the velocity field over the bed profile and (b, d, f, and h) the bed load (blue), suspended load (red), and total sediment flux (black) at (b) $t = 490$ s, (d) $t = 560$ s, (f) $t = 600$ s, and (h) $t = 670$ s.

take more time to complete and become scarce. Some larger bed forms reach a sufficient height to trap the downstream bed forms into their wake. As will be described in the following, they exert a sheltering effect on the flow and the current intensity is reduced downstream of their crests. The sediment fluxes reaching the downstream bed forms weaken, slowing down their migration until they are merged by the upstream higher bed form. Such a sequence is visible, for instance, between $t = 7000$ s and $t = 9000$ s in Figure 5.

Figure 6 shows the first part and Figure 7 the second part of one bed form merging sequence occurring before $t = 1500$ s. Figure 6 shows how a small bed form situated upstream (bed form 1) is catching up with a larger bed form situated downstream (bed form 2), which can be considered as the first stage of the merging sequence. Looking at the crests position over time (dotted black lines on Figure 6) it is clear that until $t = 300$ s bed form 1 has a higher migration velocity than bed form 2 (2.5×10^{-3} m s^{-1} instead of 1.6×10^{-3} m s^{-1}), which is due to its smaller size. The migration of bed form 1 on bed form 2 stoss side leads to bed form 2 wavelength decrease, from $\lambda = 0.3$ m to $\lambda = 0.18$ m between $t = 100$ s and $t = 300$ s. In the meantime, the height of bed form 2 is stable and so is the sediment flux at the crest. As a consequence, the sediment flux gradient over the bed form 2 reduced wavelength is increased and the height is decreased from $H = 4.6 \times 10^{-2}$ m to $H = 2.8 \times 10^{-2}$ m between $t = 300$ s and $t = 400$ s due to the higher erosion rate. Bed form 2 now migrates faster (because of the reduced height) and bed forms 1 and 2 celerities are getting closer between $t = 300$ s and $t = 400$ s (see black dotted line on Figure 6) with bed form 1 having an average celerity which is still 10% higher in this temporal interval. At $t = 400$ s, the flux profile of bed form 2 is still presenting a steep slope characterizing the ongoing erosion of the bed form.

Figure 7 shows the final stage of the bed form merging sequence. At $t = 490$ s, bed form 1 caught up with bed form 2, which has eroded since $t = 400$ s and present a flatter profile. Bed form 1 now exercises a sheltering effect on the flow, decreasing the near-bed current velocity above bed form 2 profile. As a consequence, less sediment is transported in the upstream part of the bed form 2 profile, reinforcing the crest erosion. At $t = 560$ s, both near-bed current velocity and sediment fluxes are still slowing down over bed form 2 profile. The suspension transport is almost zero, and the bed load flux has stopped upstream of the first half of bed form 2 stoss side, which lies under the influence of bed form 1 lee recirculation area. Bed form 2 profile is now split in two, upstream and downstream of the reattachment point ($x \simeq 1.32$ m). Bed form 1 is now migrating over the half inactive part of bed form 2. The downstream dune stoss side is almost flat, and the crest height has diminished by a factor 2 (compared to $t = 490$ s). At $t = 600$ s the sediment fluxes are weak (1×10^{-5} m^2 s^{-1}, which is only 10% of its original value) and the celerity of bed form 2 is close to zero. Bed form 2 is now inactive and is totally standing in bed form 1 lee recirculation zone. At $t = 670$ s, the merging sequence is completed and one final bed form is obtained. Another bed form is observed upstream and a new merging sequence is already starting. The final bed form has a height which is 50% larger than the mean height of the two former bed forms ($H \simeq 0.022$ m instead of $H \simeq 0.012$ m and $H \simeq 0.017$ m, respectively, for bed forms 1 and 2). The wavelength of the resulting bed form ($\lambda \simeq 0.25$ m) is roughly equal to the mean wavelength of the two former bed forms ($\lambda \simeq 0.18$ m and $\lambda \simeq 0.35$ m, respectively for bed forms 1 and 2). The bed form volumes before and after merging are calculated. A line is defined at the bottom of each bed form profile (red dotted lines, Figures 6a and 7g). The elevation above this line is integrated in space along the bed form profiles, $V_{\text{bed form}} = \sum_{x_s}^{x_e} h_i \Delta x_i$, where x_s and x_e define the starting and ending abscissa of the bed form, respectively. The results show that the volume of the resulting bed form after merging (3.5×10^{-3} m^2) is 20% lower than the sum of the volumes of the two former bed forms (7×10^{-4} m^2 and 3.8×10^{-3} m^2, respectively, for bed forms 1 and 2). During the merging process, bed form 2 is eroded prior to its final amalgamation by bed form 1 as evidenced in the aforedescribed sequence. As a result, 20% of the total sediment volume is lacking at the end of the merging sequence. Considering that bed form 1 has conserved its sediment, it means that almost 30% of the sediment of bed form 2 is gone. *Best et al.* [2013] also observed that the resulting bed form was not the sum of the two bed forms before merging in a flume experiment. Once the merging sequence is completed, the wavelength of the resulting bed form is adjusting to the new crest height, and having more space to develop, will slowly increase, as can be seen, for example, after a merging sequence at $t = 6000$ m (see Figure 5).

Another phenomenon is also clearly visible on Figure 5: Around $t \simeq 2500$ s, $t \simeq 4500$ s and $t \simeq 7500$ s temporal striations are observed on the dune profiles. This is the signature of the degeneration of the dune crest (sometimes referred to as dune splitting) and is remarkably similar to observations in the experimental study of *Martin and Jerolmack* [2013]. This phenomenon is linked to the presence of superimposed bed forms and will be detailed in section 4.3.

Figure 8 shows the temporal evolution of the statistical mean wavelength, $< \lambda >$, and height, $< H >$, of the bed form field. It can be seen that $< H >$ and $< \lambda >$ increase at a rapid pace until $t \simeq 3500$ s. After $t = 3500$ s the evolution is slower, which is due to the fact that the bed forms are getting larger, have a lower celerity, and merging sequences become scarce. For $t \geq 6500$ s, the mean wavelength reach an asymptote value, but several bed forms of different sizes are still present on the domain (see Figure 5). The dune field
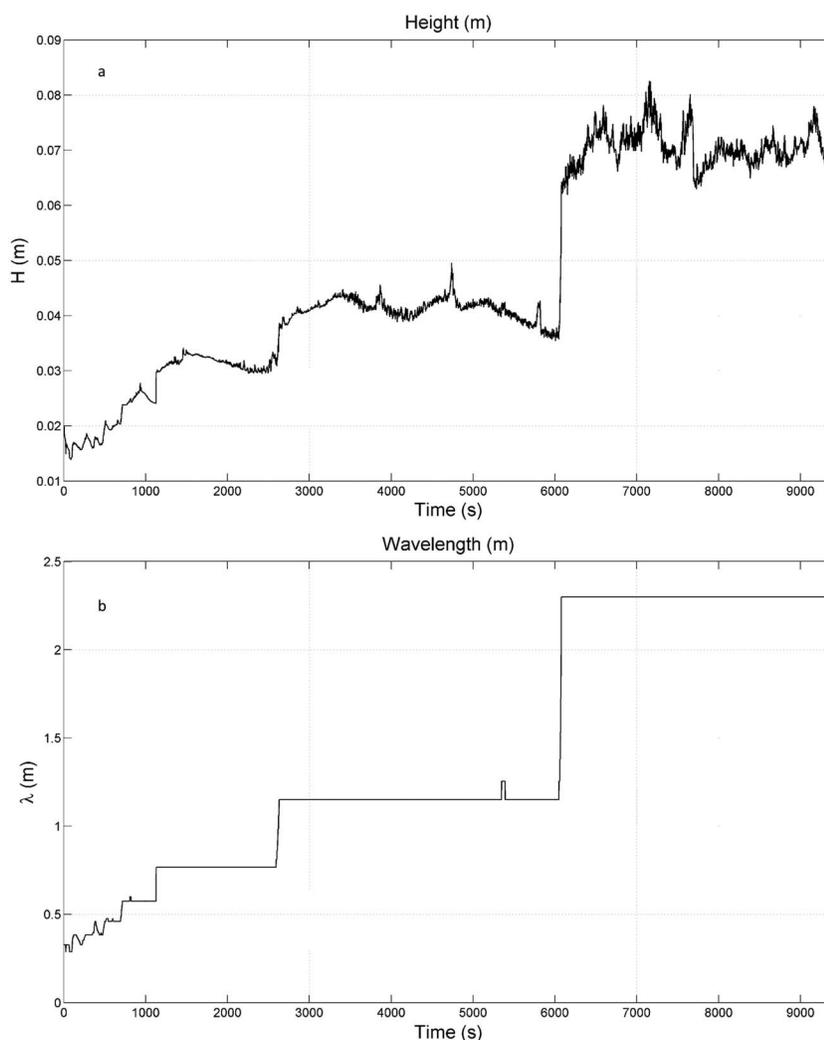
Figure 8. (a) Time series of the evolution of the mean height, $<H>$, and (b) time series of the evolution of the mean wavelength, $<\lambda>$.

saturation occurs only after the last merging sequences, around $t = 9000$ s. These results are in good agreement with *Naqshband et al.* [2014] experiment. They observed $<H>$ and $<\lambda>$ growing rapidly until approximately $t = 3600$ s, then the bed evolving slowly until saturation was reached at $t = 9000$ s. The model performances are very good concerning the dune field characteristics at equilibrium. At equilibrium, the simulation results show a dune field of $<\lambda> = 2.3$ m and $<H> \simeq 0.075$ m. The maximum height is reached around $t = 7000$ s with $<H> \simeq 0.083$ m. In the experiment of *Naqshband et al.* [2014], the dune field had a mean wavelength of $<\lambda> = 2.27$ m and a mean height of $<H> = 0.082$ m at equilibrium. The slight difference between the simulated and experimental mean heights at equilibrium (8%) can be attributed to the variation of the water depth during the experiment. Flumes studies show that as the dunes grow, more resistance is generated and the water depth increases [*Simons and Richardson*, 1962]. In *Naqshband et al.* [2014] experiment, the water depth was monitored and maintained at $D_0 = 0.25$ m with a precision of 10%, which leads to an error margin of the same order of magnitude on the dune height, as it is re-adapting to the water depth. The average dune migration velocity at saturation is $c_e \simeq 8.10^{-4}$ m.s^{-1} in the simulation, which is also very similar to the experimental results, $c_e \simeq 7 \times 10^{-4}$ m s^{-1} of *Naqshband et al.* [2014].

The suspension load is of the same order of magnitude as the bed load over migrating dunes at equilibrium, although the transport is dominated by the bed load. The suspended load has an intensity of roughly 30% of that of the bed load, which is in good agreement with values in [*Naqshband et al.*, 2014] experimentation. Both suspended load and bed load arriving at the crest contribute to sand dunes migration.
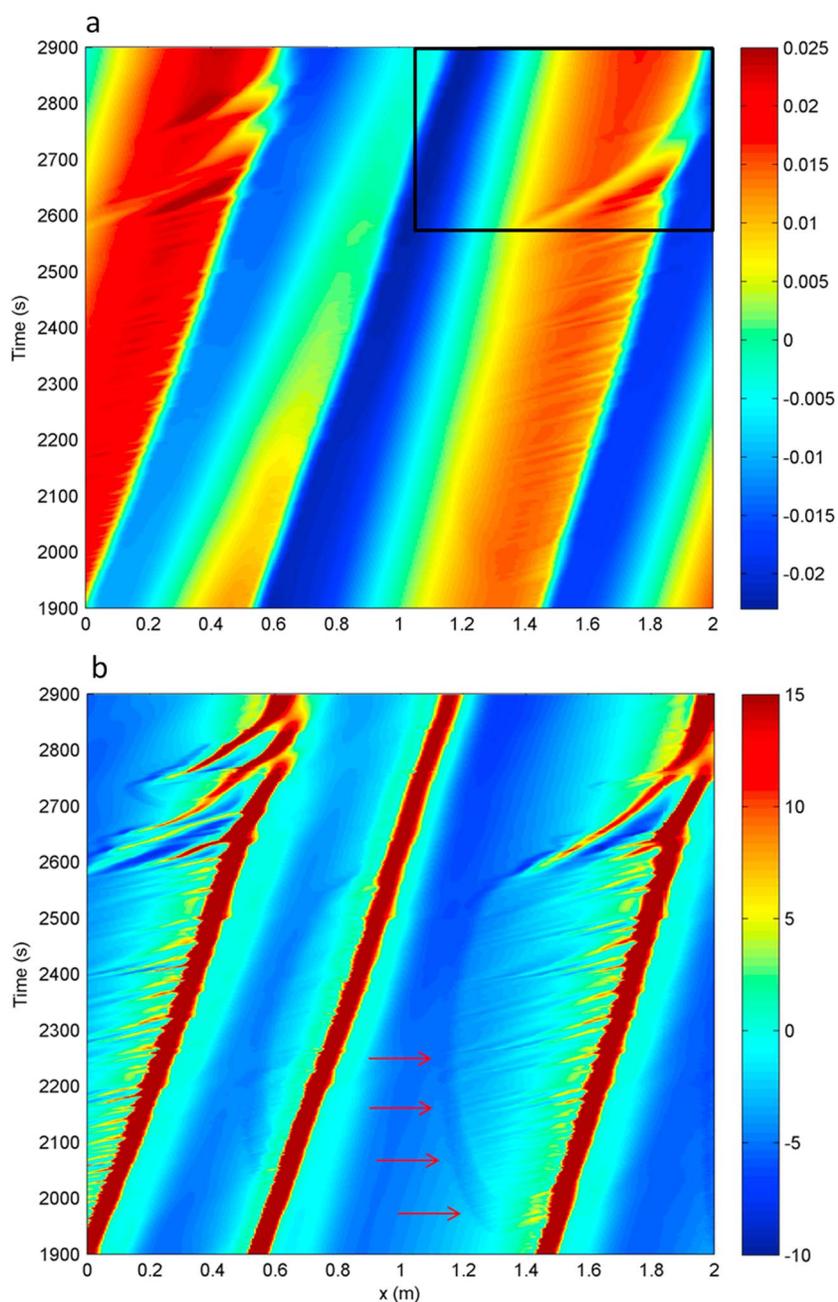
Figure 9. Time evolution of (a) the bed height, and (b) the bed slope (in degrees) from the zoomed-in subset in Figure 5. The red arrows indicate the position of the dune stoss slope deflection.

4.3. Superimposed Bed Forms
4.3.1. Observation

Superimposed bed forms are observed on the dune profiles during the experimentation of *Naqshband et al.* [2014]. Moreover, in a time lapse of the same experiment (S. Naqshband, personal communication, 2014), superimposed bed forms are generated while an upstream dune is being merged. Alternate periods with and without superimposed bed forms on the stoss side of the dunes were observed, which is also the case in the numerical simulation.

Figure 9 shows a zoomed-in subset (see Figure 5) of the bed elevation and bed slope on one of the afore-mentioned areas where temporal striations in the bed profile were noticed ($t = 1900$ s to $t = 2900$ s). The origin coordinate of the abscissa axis is shifted by 2.6 m to the right to better visualize the phenomenon

described below. It is obvious from Figure 9a that some perturbations are developing on the stoss side of the dune and getting larger with time. As they are migrating toward the dune crest, these superimposed bed form perturbations develop into ripples that are 1 order of magnitude smaller than the equilibrium dunes. One larger superimposed bed form that is generated on the stoss side of the dune eventually provokes the degeneration of the dune crest between $t = 2600$ s and $t = 2750$ s.

The bed slope temporal evolution (Figure 9b) shows that the bed forms are generated at a location where the dune stoss slope exhibits a slight deflection. The position of the slope discontinuity varies on the profile and propagates upstream between $t = 1990$ s and $t = 2550$ s describing a crescent shaped trajectory on Figure 9b. The distance between the generation point and the dune crest increases, allowing larger and higher superimposed bed forms. The last bed forms migrate during 200 s over a distance of 0.8 m before they reach the crest. Interestingly, while superimposed bed forms are emerging on the dune stoss side, the height of the upstream dune is concomitantly decreasing, as it is being shadowed by a larger dune as described in section 4.2.

4.3.2. Generation Mechanism

To verify the hypothesis that a deflection in the slope can potentially generate superimposed bed forms, a test was carried out with two idealized dune profiles (Figure 10). The first dune profile is triangular shaped (Figure 10a) and the second is nearly the same but exhibits a slight deflection in the stoss side slope (Figure 10b). This slope deflection equals 1°, which is the order of magnitude of that observed in (Figure 9b). The dune profile magnitude and the hydrodynamic forcing are those used for the previous simulation (see Table 1), but for the sake of simplicity, only the bed load flux is taken into account in the simulations.

The results of the bed evolution against time for both configurations are shown in Figure 10. The first dune profile remains stable and no perturbations are noticed on the dune stoss side, whereas superimposed bed forms quickly arise on the second dune profile, colonizing the upper part of the dune stoss side downstream of the deflection. To understand how superimposed bed forms are generated at the stoss slope deflection, the fluxes are calculated and represented in Figure 11, at different times. Clearly, some fluxes perturbations arise, growing with time and propagating downstream toward the crest. The small sediment transport perturbation induced by the slope deflection, of 1°, is sufficient to initiate the generation of small bed forms that grow with time. After $t = 100$ s a field of well-developed superimposed bed forms is present over the dune stoss side.

4.3.3. Origin of the Slope Deflection

Figure 9a shows that concomitantly to the emergence of the slope deflection and superimposed bed forms on the dune stoss side, the upstream dune height is gradually diminishing. In the following we study the link between the reduction of the upstream dune height and the emergence of the slope deflection through the analysis of the turbulence relaxation.

An additional simulation was carried out in order to highlight the effect of the reduction of the upstream dune height. The bed form is extracted at $t=1850$ s in the main simulation, when no superimposed bed forms are present on the dune profile. This is the reference profile, called scenario 1 in the following. The same profile but with a reduction of the upstream dune height by ∼25% is called scenario 2 in the following. This height reduction corresponds to the order of magnitude of the upstream dune height decrease observed in the main simulation at $t=2250$ s (Figure 9a). Figure 12 shows the comparison between scenario 1 and scenario 2 under the same forcing conditions (see Table 1), in order to assess the impact of dune height reduction on the hydrodynamics and sediment transport. In Figures 12a and 12b, the turbulent kinetic energy field is shown for both scenarios. The lower dune (scenario 2) generates a smaller plume which extends on a much shorter distance. Figure 12c shows that the mean turbulence in the water column, k_m, for scenario 2, is reduced by almost 15% compared to scenario 1.

Fredsøe [1982], by analogy with the flow behind a backward facing step, explained the effect of the boundary layer turbulent relaxation on the distribution of the bed friction, c_f. In a train of dunes, the turbulent relaxation sets the spatial distribution of c_f, downstream of the crests [*Tjerry and Fredsøe*, 2005].

As the amount of turbulence diminishes in the water column, the bed friction c_f increases from almost zero (at $x = 0.6$ m) to a maximum value, near the dune crest (Figure 12d, scenario 1). At this location, the amount of turbulence in the water column is too low to impact the bed friction, it is the end of the turbulence relaxation zone. Let us define l_r, the turbulence relaxation length, starting from the upstream crest to the end of the turbulence relaxation zone. l_r, in scenario 2, is about half of the value in scenario 1 (Figure 12c), which leads to
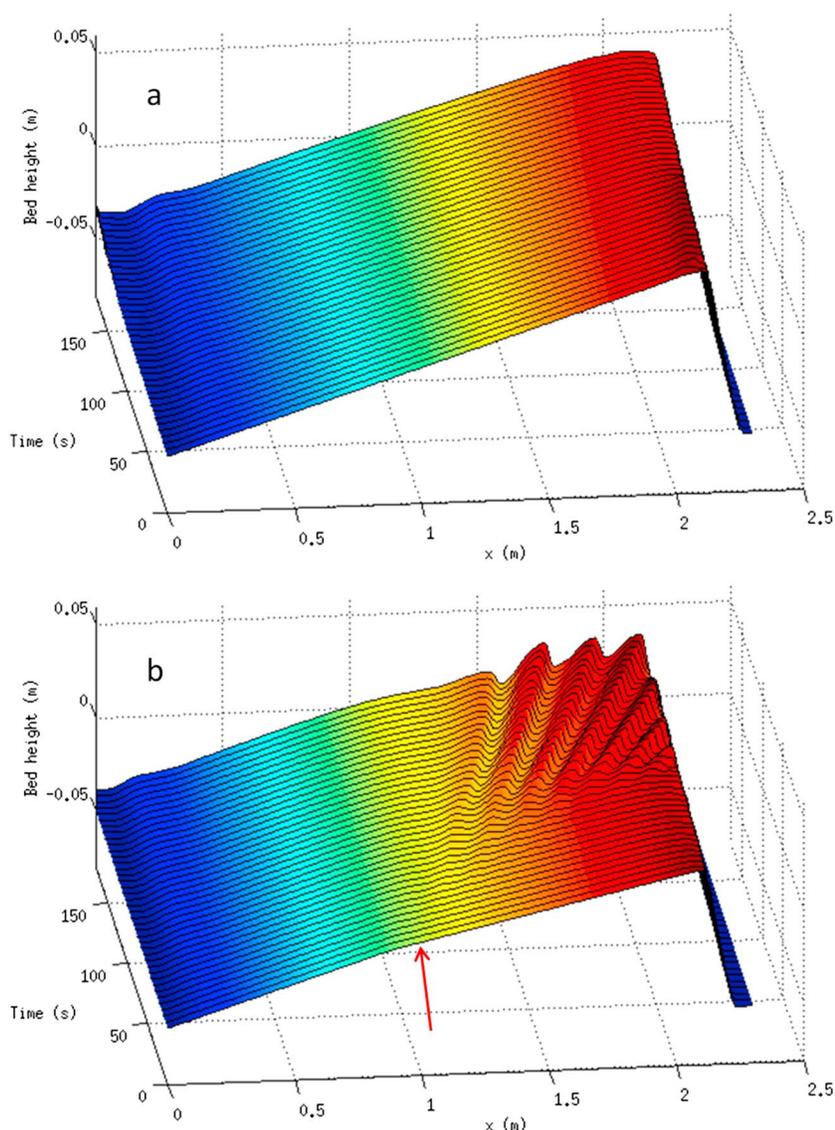
Figure 10. (a) Time evolution of an idealized triangular-shaped dune and (b) time evolution of an idealized triangular-shaped dune presenting a deflection of 1° (pointed by a red arrow) in the stoss side slope. The vertical scale is exaggerated 10 times and the red arrow shows the position of the slope deflection.

larger values of c_f for scenario 2 (Figure 12d). According to *Tjerry and Fredsøe* [2005], the bottom shear stress is related to c_f by

$$\tau_b = \rho c_f U^2, \tag{11}$$

where U is the depth-integrated average flow velocity and c_f is the bottom friction coefficient. Equation (11) means that the variation of τ_b, and therefore of the local Shields number θ, is linked to the relaxation of the turbulence, through c_f. As a consequence, the upstream crest height diminution leads to perturbations of the sediment flux gradient on a distance l_r from the upstream crest, as shown in Figure 12e, which leads to a disequilibrium in the sediment migration velocity on this zone. Eventually, this process leads to a sediment accumulation on the lower part of the dune stoss side, which creates a slope deflection. The value found for l_r in scenario 2 corresponds roughly to the localization of the slope deflection at $t \sim 2250$ s in the simulation (upper red arrow on Figure 9b), when the upstream dune height was similar to scenario 2. As shown on Figure 9b, while the upstream dune crest height is decreasing, the slope deflection propagates upstream from the top to the bottom of the dune stoss side. The position of the slope deflection follows the position of the
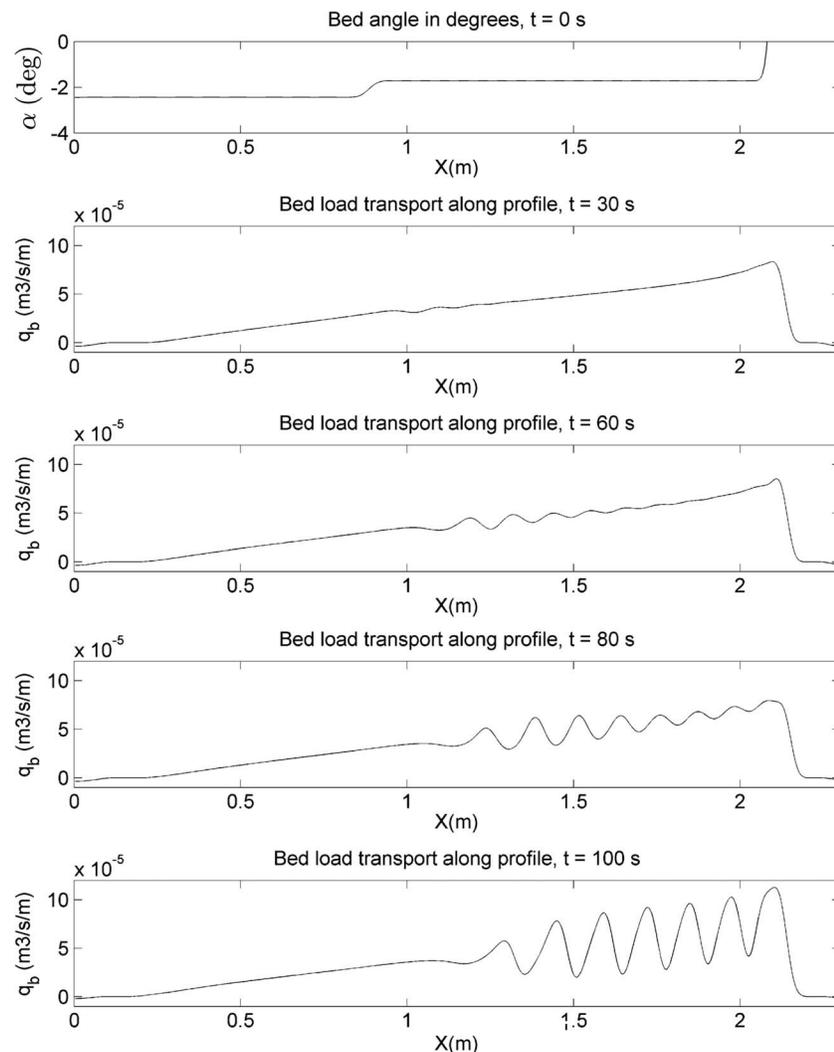
Figure 11. Initial bed slope angle (α) and bed load transport (q_b) along the dune profile from $t = 30$ s to $t = 100$ s for an idealized dune presenting a 1° deflection in its stoss side slope.

relaxation length, as shown on Figure 13. Figure 13 also shows that the deflection disappears after $t = 2650$ s, as the turbulent field has become very weak.

This adaptation of the dune profile to the upstream dune height decrease allows the superimposed bed forms to develop on a larger distance. The occurrence of the superimposed bed forms can be interpreted as being the signature of a disequilibrium between two consecutive bed forms within the bed forms field. The superimposed bed forms immediately downstream of the deflection point exhibit a wavelength of the same order of magnitude as the incipient ripples and are of the same nature ($\lambda \simeq 0.07 - 0.08$ m, section 4.1).

The physical processes described in this section show an additional mechanism of emergence of superimposed bed forms besides turbulent bursting [*Raudkivi*, 1997; *Nabi et al.*, 2013]. *Nabi et al.* [2013] showed that turbulence jets are able to generate these bed forms but the simulation suggests that it is not a necessary condition as superimposed bed forms are generated within the process of self-organization of the bed. Also, it is still not clear whether turbulence triggers the initial perturbations leading to the formation of ripples [*Kuru et al.*, 1995; *Coleman and Eling*, 2000; *Venditti et al.*, 2006]. *Niemann* [2011] simulated the effect of excess of turbulent intensity and found insignificant impact on the bed form shape. Moreover, *Venditti et al.* [2005b] observed in their experimental study that superimposed sand sheets were generated at a location much farther away than the point of reattachment where the turbulent fluctuations are believed to initiate the perturbations.
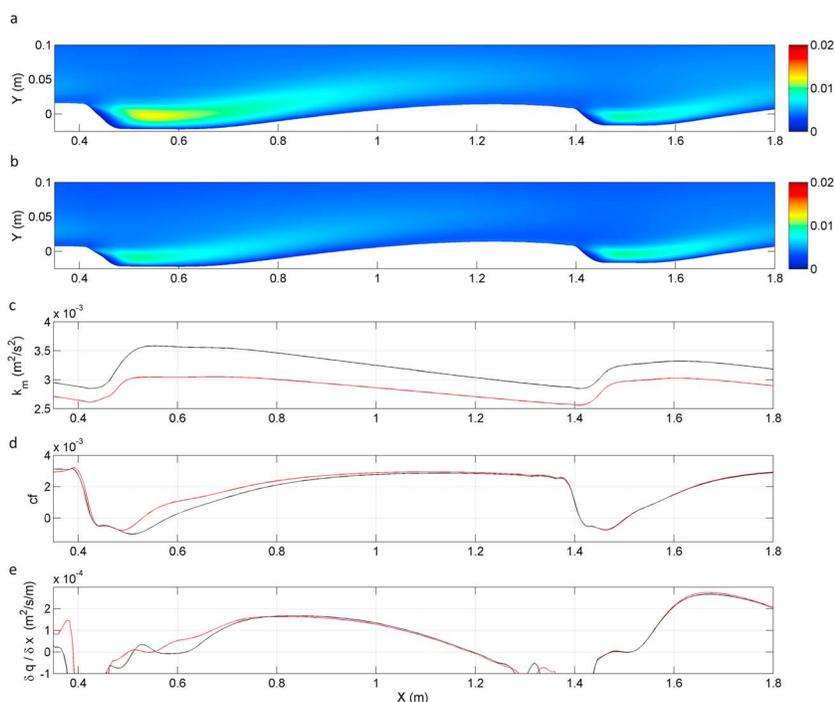
Figure 12. (a) Turbulent kinetic energy field k at $t = 1850$ s for the baseline simulation (scenario 1) and (b) with a 25% lower upstream dune (scenario 2) with the corresponding spatial evolution of (c) the mean turbulence in the water column, k_m, (d) the skin friction coefficient c_f, and (e) the total transport gradient $\Delta q / \Delta x$ for scenario 1 (black) and scenario 2 (blue).

4.4. Dune Degeneration

The superimposed bed forms generated on the stoss side grow with time, sometimes merging with each other. They potentially provoke the degeneration of the dune crest in the simulation as is the case for $2650 \leq t \leq 2700$ s (see Figure 9). To analyze the mechanism of dune degeneration a sequence of four instantaneous bed profiles was extracted from the simulation, with the associated velocity field and sediment fluxes (Figure 14).

At $t = 2600$ s, two superimposed bed forms are present upstream of the crest. The upstream smaller ripple has just emerged and has the characteristics of an incipient ripple (cf. section 4.1), whereas the downstream ripple has a wavelength more than twice larger ($\lambda \simeq 0.2$ m). The sediment flux along the large superimposed bed form profile is of the same order of magnitude as the fluxes at the dune crest (bed load and suspension). In the wake of both superimposed bed forms crests, the transport is dramatically lowered due to the sheltering effect on the flow (by 60% and 75% for the upstream and the downstream ripple, respectively). As a consequence, less sediment is transiting to the dune crest, and the high fluxes gradients just upstream of the crest (1.65 m $< x < 1.75$ m) lead to its erosion. At $t = 2640$ s, the transport has lowered by 65% over the dune crest, which stalls, and the dune lee recirculation zone is reduced. At $t = 2700$ s the superimposed ripple merge with the dune crest and a new dune front is created. Also, the lee recirculation zone is restored. For $t > 2800$ s the dune has reformed but with a quite different shape. The position of the superimposed ripples ($\lambda \simeq 0.2$ m, $KD_0 \simeq 7.9$) is shown on the (KD_0, Fr) diagram in Figure 1.

Figure 15 shows a comparison between the profile at $t = 1900$ s before the superimposed bed forms have developed and at $t = 2800$ s after the crest has just recovered. The new profile is less steep at the crest than the original profile, the lee slope is no longer equal to the sediment angle of repose. The brink height of the resulting dune is 20% lower and the crest position relative to the brink position has moved backward over the profile to a distance increased by 30%. The dune wavelength has increased by 10% from $\lambda \simeq 0.82$ m to $\lambda \simeq 0.9$ m.

The resulting dune profile is exhibiting a smoother and longer profile, which is a geometrical characteristic of a lower angle dune in the absence of an upstream relaxation, as described in *Tjerry and Fredsøe* [2005].
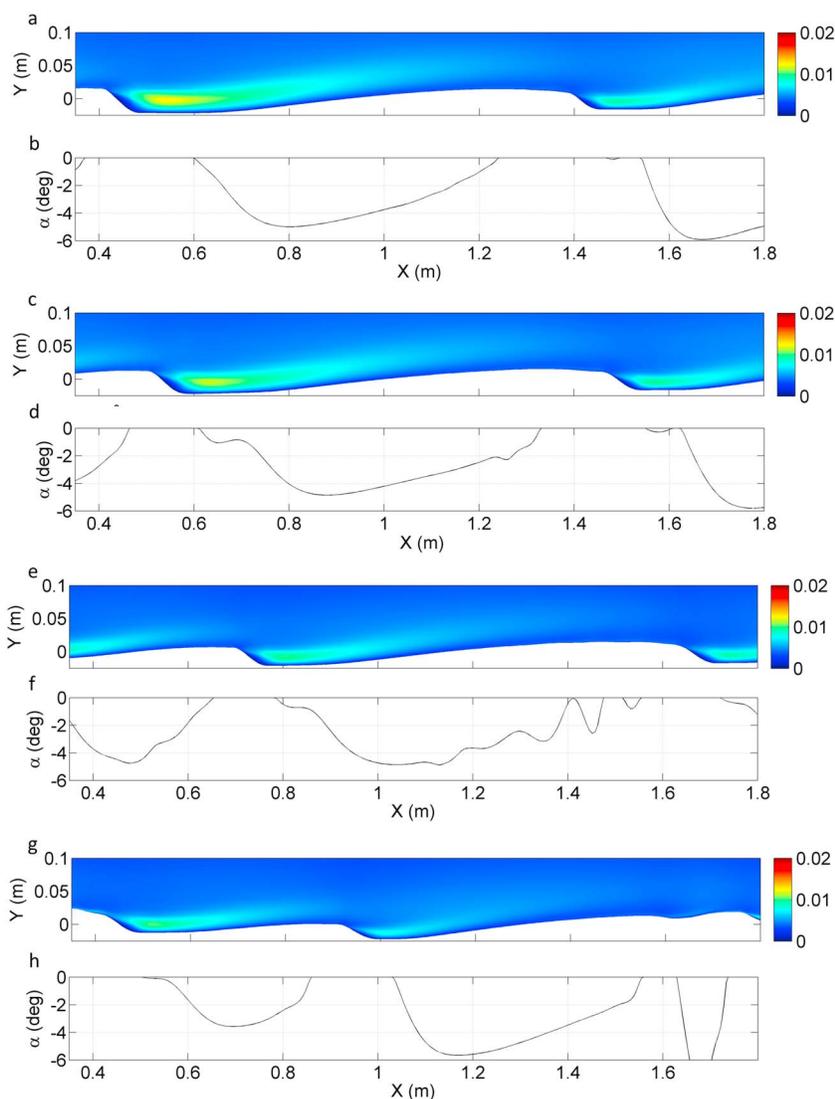
Figure 13. Deflection shifting sequence with (a, c, e, and g) the turbulent kinetic energy field, k, and the bed slope along the bed profile, α, at (b) $t = 1850$ s, (d) $t = 2000$ s, (f) $t = 2300$, and (h) $t = 2650$ s. Higher values at the crest are not shown for a better visualization.

The profile curvature effects become important, and the maximum of friction is moved farther downstream, resulting in a longer dune. Lower angle dunes are usually obtained for lower Shields numbers where the diffusion effects of gravity are relatively high [*Niemann*, 2003]. By provoking the degeneration of the dune crest, superimposed bed forms play an active role in the transition between the original dune profile and the smoother dune profile. Based on these results, it can be concluded that dunes within a dune field will exhibit different shapes depending on the upstream bed form dimensions. Also, it suggests that under equivalent hydrodynamic conditions, solitary dunes will exhibit lower angle profiles.

The results show that there exists a threshold height above which the superimposed ripples are able to provoke the degeneration of the crest of the principal dune. Before $t = 2600$ s, the smaller superimposed bed forms are collapsing by provoking avalanches when reaching the dune crest. After $t = 2600$ s, the dune crest degenerates and is eventually merged with the closest superimposed bed form. This means that there exists a critical height above which the ripple provoke the dune crest degeneration. In this simulation, the superimposed bed form has a height of $H = 0.009$ m at $t = 2640$ s while it is merging with the dune crest, which represents ~28% of the dune height (0.032 m). This result is consistent with the results of *Warmink et al.* [2014] and *Reesink and Bridge* [2009] who obtained 21% and 25% ratios, respectively, in their experiment with dunes of comparable dimensions. *Warmink et al.* [2014] describe the sequence as being a dune splitting but during
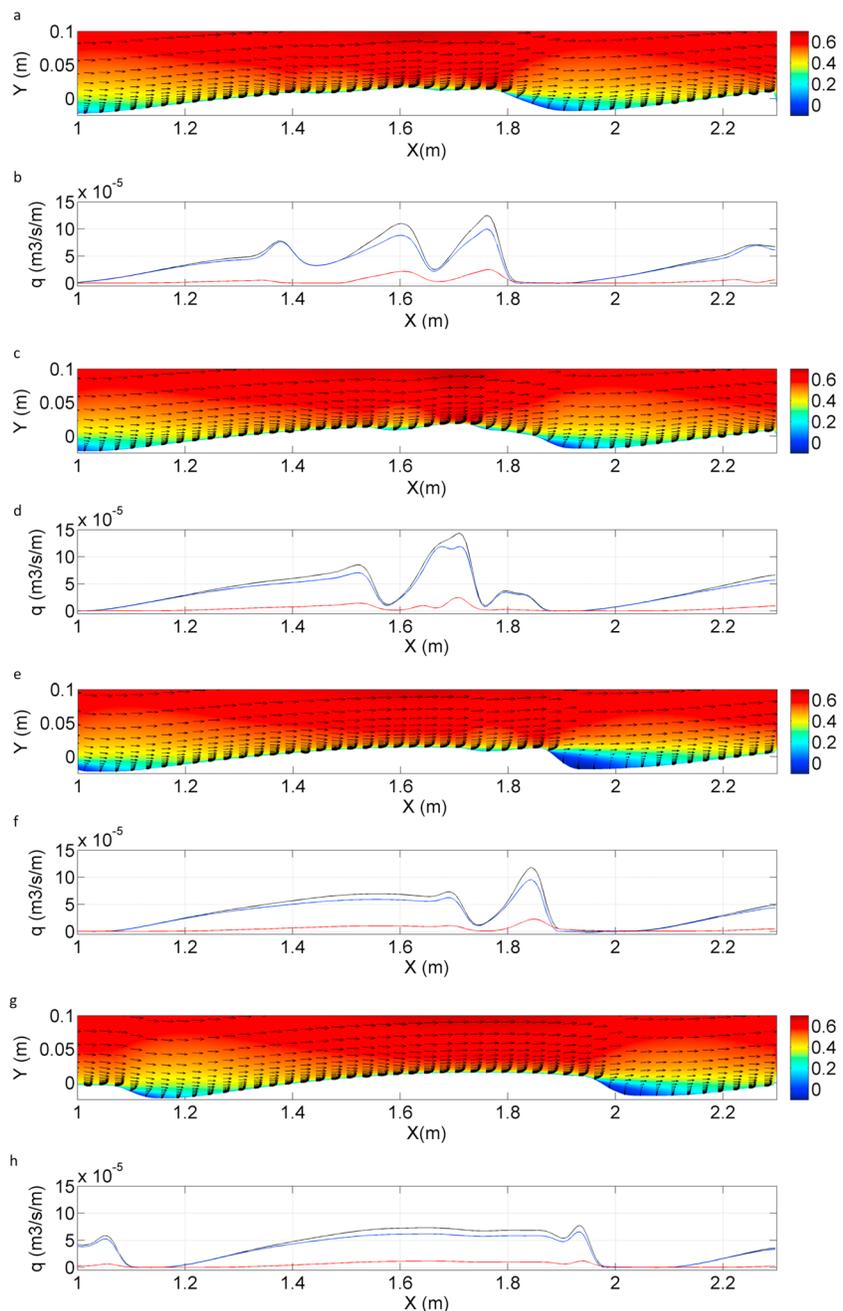
Figure 14. Crest degeneration sequence occurring in the zoomed-in subset of Figure 9, with (a, c, e, and g) the velocity field over the bed profile and the bed load (blue), suspended load (red), and total sediment flux (black) at (b) $t = 2600$ s, (d) $t = 2640$ s, (f) $t = 2700$ s, and (h) $t = 2900$ s.

the process the dune crest merges with the superimposed bed form and does not survive in the form of a smaller bed form. This is the reason why the expression "dune degeneration" is preferred herein.

The simulation results show that degeneration of the dune crest is the ultimate consequence of the disequilibrium initiated by the shrinking of the upstream bed form. This configuration occurs at regular time intervals within the simulation and is an important factor of generation of superimposed bed forms. These results show that superimposed bed forms are a key mechanism of sand dune evolution: Not only can they induce bed roughness and high modifications on the sediment fluxes but they can also force the degeneration of larger dunes and modify their profile, which can potentially lead to dune splitting as observed in nature by *Jerolmack and Mohrig* [2005].
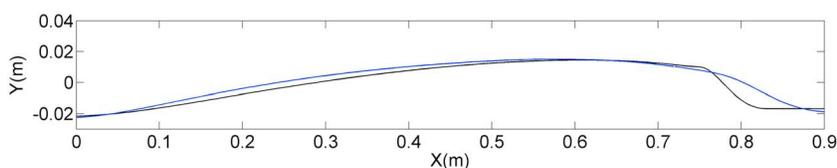
Figure 15. Dune profile at t = 1900 s (black), before the superimposed bed forms development and at t = 2800 s (blue), after the crest has reformed.

5. Conclusions

A 2-D RANS model was employed to study the evolution of an erodible and noncohesive sand bed submitted to a stationary unidirectional current. Careful monitoring of the model stability and of the resolution insured the consistency of the results. Moreover, the high near-bed resolution guaranteed a good description of the subviscous layer dynamics. The model was able to simulate the evolution of an initially flat sand bed through various distinct phases, which are the linear incipient ripple generation, the nonlinear ripple growing phase, and the fully developed dune evolution with superimposed bed form.

The initial phase of incipient ripples generation was successfully reproduced, and results are in line with both analytical models and experimentations. The dominant ripple wavelength related to the sand rugosity was especially well reproduced. We showed that the initial phase consists of two stages: in the early stages the small perturbations are exponentially growing in height, then after a rapid period of tens of seconds the nascent ripples are equilibrating with each other giving birth to the initial ripple field. The presence of a recirculation zone was not a necessary condition for the development and migration of the first perturbations, but appeared at a later stage while ripples are equilibrating with each other. This work showed the ability of this numerical model to reproduce the initial phase of ripple generation and opens new perspectives for a more exhaustive analysis of initial ripple fields for a broader range of conditions.

Beyond the initial linear phase, the simulation of the nonlinear bed evolution compared well with an experiment. The results showed that the bed growth is insured by cascading bed form merging sequences until equilibrium. The bed form merging occurred in two steps: first, smaller bed forms of higher migration velocities catch up with larger downstream bed forms, then the downstream bed forms collapse due to the shadowing of the upstream bed forms. During the process, the mean bed form height increases but the mean wavelength remains relatively unchanged. The mean wavelength then gradually grows, to readjust to the new heights of the merged bed forms. The model reproduces well the merging mechanism and the simulation results provide a better understanding of how merging is driving the bed growth by increasing the individual bed form heights.

During the simulation, superimposed bed forms emerged on the dune stoss sides similarly to previous experimental observations. An analysis of their generation mechanism has shown that superimposed bed forms were emerging downstream of a slight deflection in the dune profile slope. The deflection was found to be the consequence of the reduced intensity of the upstream turbulence relaxation length, due to the gradual reduction of the upstream bed form height. As they travel over the dune stoss side, superimposed bed forms grow and eventually provoke the degeneration of the dune crest. The resulting dune exhibits a smoother profile, which is characteristic of a lower angle dune and therefore highlights the difference between solitary dunes and dunes within a field under the same hydrodynamic conditions. The bed growth is slowed down under the action of superimposed bed forms. It can be concluded from these results that the bed evolution is driven by two main antagonistic physical processes: bed form merging sequences insuring the bed form growth and superimposed bed forms slowing down the bed growth by provoking dune degeneration and splitting. As such, superimposed bed forms also play a major role in the bed self-organization processes, suggesting that they tend to homogenize the bed form field.

References

Andersen, K. H. (1999), The dynamics of ripples beneath surface waves and topics in shell models of turbulence, PhD thesis, Det Naturvidenskabelige Fakultet Københavns Universitet. [Available at http://www.nbi.dk/kenand/Thesis.html.]
Ashley, G. M. (1990), Classification of large-scale subaqueous bedforms: A new look at an old problem, *J. Sediment. Petrol.*, *60*, 160–172.
Baas, J. H. (1994), A flume study on the development and equilibrium morphology of current ripples in very fine sand, *Sedimentology*, *41*, 185–209.

Baas, J. H. (1999), An empirical model for the development and equilibrium morphology of current ripples in fine sand, *Sedimentology*, *46*, 123–138.

Bagnold, R. R. (1941), *The Physics of Blown Sand and Desert Dunes*, Chapman and Hall, London.

Barrie, J. V., and K. W. Conway (2014), Seabed characterization for the development of marine renewable energy on the Pacific margin of Canada, *Cont. Shelf Res.*, *83*, 45–52, doi:10.1016/j.csr.2013.10.016.

Bennett, J., and J. Best (1995), Mean flow and turbulence structure over fixed, two-dimensional dunes: Implications for sediment transport and bedform stability, *Sedimentology*, *42*, 491–513.

Best, J. (1992), On the entrainment of sediment and initiation of bed defects: Insights from recent developments within turbulent boundary layer research, *Sedimentology*, *39*, 797–811, doi:10.1111/j.1365-3091.1992.tb02154.x.

Best, J. (2005), The fluid dynamics of river dunes: A review and some future research directions, *J. Geophys. Res.*, *110*, F04S02, doi:10.1029/2004JF000218.

Best, J., G. Blois, J. Barros, and K. Christensen (2013), The dynamics of bedform amalgation: New insights from a very thin flume, in *Proceeding of Marine and River Dune Dynamics MARID IV*, pp. 29–34, SHOM, Bruges, Belgium.

Betat, A. (1999), Sand ripples induced by water shear flow in an annular channel, *Phys. Rev. Lett.*, *83*, 88–91.

Betat, A., C. A. Kruelle, V. Frette, and I. Rehberg (2002), Long-time behavior of sand ripples induced by water shear flow, *Eur. Phys. J. E*, *8*, 465–476, doi:10.1140/epje/i2001-10110-y.

Boothroyd, J. C., and D. K. Hubbard (1975), *Genesis of Bedforms in Mesotidal Estuaries*, edited by L. E. Cronin, pp. 217–234, Estuarine Research, Academic Press, New York.

Charru, F., and H. Mouilleron-Arnould (2002), Instability of a bed of particles sheared by a viscous flow, *J. Fluid Mech.*, *452*, 303–323.

Charru, F. (2006), Selection of the ripple length on a granular bed sheared by a liquid flow, *Phys. Fluids*, *18*, 121508, doi:10.1063/1.2397005.

Charru, F., and E. Hinch (2006), *J. Fluid Mech.*, *550*, 111–121, doi:10.1017/S002211200500786X.

Charru, F., B. Andreotti, and P. Claudin (2013), Sand ripples and dunes, *Annu. Rev. Fluid Mech.*, *45*, 469–493, doi:10.1146/annurev-fluid-011212-140806.

Coleman, S. E., and B. Eling (2000), Sand wavelets in laminar open-channel flows, *J. Hydraul. Res.*, *38*, 331–338.

Coleman, S. E., and B. W. Melville (1994), Bed-form development, *J. Hydraul. Eng.*, *120*, 544–560.

Coleman, S. E., and B. W. Melville (1996), Initiation of bed forms on a flat sand bed, *J. Hydraul. Eng.*, *122*, 301–310.

Coleman, S. E., J. J. Fedele, and M. H. Garcia (2003), Closed conduit bed form initiation and developpment, *J. Hydraul. Eng.*, *129*, 956–965.

Colombini, M. (2004), Revisiting the linear theory of sand dune formation, *J. Fluid Mech.*, *502*, 1–16, doi:10.1017/S0022112003007201.

Colombini, M., and A. Stocchino (2011), Ripple and dune formation in rivers, *J. Fluid Mech.*, *673*, 121–131, doi:10.1017/S0022112011000048.

Dalrymple, R. W., J. R. Knight, and J. J. Lambiase (1978), Bedforms and their hydraulic stability relationships in a tidal environment, Bay of Fundy, Canada, *Nature*, *275*, 100–104.

Engelund, F. (1966), Hydraulic resistance of alluvial streams, *HY4*, 287–297.

Engelund, F. (1970), Instability of erodible beds, *J. Fluid Mech.*, *42*, 225–244.

Engelund, F., and J. Fredsøe (1976), A sediment transport model for straight alluvial channels, *Nord. Hydrol.*, *7*, 293–306.

Eriksson, L. E. (1982), Generation of boundary-conforming grids around wing-body configurations using transfinite interpolation, *AIAA J.*, *20*, 1313–1320.

Fourrière, A., P. Claudin, and B. Andreotti (2010), Bedforms in a turbulent stream: Formation of ripples by primary linear instability and of dunes by nonlinear pattern coarsening, *J. Fluid Mech.*, *649*, 287–328, doi:10.1017/S0022112009993466.

Fredsøe, J. (1974), On the development of dunes in erodible channels, *J. Fluid Mech.*, *64*, 1–16, doi:10.1017/S0022112074001960.

Fredsøe, J. (1982), Shape and dimensions of stationary dunes in rivers, *J. Hydraul. Div.*, *8*, 932–947, doi:10.1017/S0022112074001960.

Fredsøe, J., and R. Deigaard (1992), *Mechanics of Coastal Sediment Transport*, pp. 369 pp., World Scientific, N. J.

Giri, S., and Y. Shimizu (2006), Numerical computation of sand dune migration with free surface flow, *Water Resour. Res.*, *42*, W10422, doi:10.1029/2005WR004588.

Guy, H., D. Simons, and E. Richardson (1966), Summary of alluvial channel data from flume experiments 1956–1961, *U.S. Geol. Surv. Prof. Pap., 462-I*.

Jerolmack, D. J., and D. Mohrig (2005), A unified model for subaqueous bed form dynamics, *Water Resour. Res.*, *41*, W12421, doi:10.1029/2005WR004329.

Kennedy, J. F. (1963), The mechanics of dunes and antidunes in erodible-bed channels, *J. Fluid Mech.*, *16*, 521–544.

Kuru, W. C., D. T. Leighton, and M. J. McReady (1995), Formation of waves on a horizontal erodible bed of particles, *Int. J. Multiphase Flow*, *21*, 1123–1140.

Langlois, V., and A. Valance (2007), Initiation and evolution of current ripples on a flat sand bed under turbulent water flow, *Eur. Phys. J. E*, *22*, 201–208.

Leclair, S. F. (2002), Preservation of cross-strata due to the migration of subaqueous dunes: An experimental investigation, *Sedimentology*, *49*, 1157–1180.

Mantz, P. A. (1978), Bedforms produced by fine, cohesionless, granular and flakey sediments undersubcritical water flows, *Sedimentology*, *25*, 83–103.

Marieu, V., P. Bonneton, D. L. Foster, and F. Ardhuin (2008), Modeling of vortex ripple morphodynamics, *J. Geophys. Res.*, *113*, C090007, doi:10.1029/2007JC004659.

Martin, R. L., and D. J. Jerolmack (2013), Origin of hysteresis in bed form response to unsteady flows, *Water Resour. Res.*, *49*, 1314–1333, doi:10.1002/wrcr.20093.

McLean, S. R. (1990), The stability of ripples and dunes, *Earth Sci. Rev.*, *29*, 131–144.

Meyer-Peter, E., and R. Müller (1948), Formulas for bed-load transport, in *Proc. Int. Assoc. Hydraul. Res., 3rd Ann. Conference*, pp. 39–64, Stockholm.

Nabi, M., H. J. D. Vriend, E. Mosselman, C. J. Sloff, and Y. Shimizu (2013), Detailed simulation of morphodynamics: 3. Ripples and dunes, *Water Resour. Res.*, *49*, 1–14, doi:10.1002/wrcr.20457.

Naqshband, S., J. S. Ribberink, D. Hurther, and S. J. M. H. Hulscher (2014), Bed load and suspended load contributions to migrating sand dunes in equilibrium, *J. Geophys. Res. Earth Surface*, *119*, 1043–1063, doi:10.1002/2013JF003043.

Naqshband, S., J. S. Ribberink, D. Hurther, P. A. Barraud, and S. J. M. H. Hulscher (2015), Experimental evidence for turbulent sediment flux constituting a large portion of the total sediment flux along migrating sand dunes, *Geophys. Res. Lett.*, *41*, 8870–8878, doi:10.1002/2014GL062322.

Nelson, J. M., R. M. Lean, and S. R. Wolfe (1993), Mean flow and turbulence fields over two-dimensional bed forms, *Water Resour. Res.*, *29*, 3935–3953.

Niemann, S. L. (2003), Modelling of sand dunes in steady and tidal flow, PhD thesis, Tech. Univ. of Copenhagen.

Niemann, S. L. (2011), Sand dunes in steady flow at low Froude numbers: Dune height evolution and flow resistance, *J. Hydraul. Eng.*, *137*, 5–14, doi:10.1061/(ASCE)HY.1943-7900.0000255.

Nikuradse, J. (1933), *Strmungsgesetze in Glatten und Rauhen Rohren*, VDI Forschungsheftr 361, Berlin.

Paarlberg, A. J., C. M. Dohmen-Janssen, and S. J. Hulscher (2009), Modeling river dune evolution using a parameterization of flow separation, *J. Geophys. Res.*, *114*, F01014, doi:10.1029/2007JF000910.

Patankar, S. V. (1980), *Numerical Heat Transfer and Flow*, Hemisphere, New York.

Perillo, M. M., J. L. Best, M. Yokokawa, T. Sekiguchi, T. Takagawa, and M. H. Garcia (2014), A unified model for bedform development and equilibrium under unidirectional, oscillatory and combined-flows, *Sedimentology*, *61*, 2063–2085, doi:10.1111/sed.12129.

Raudkivi, A. J. (1997), Ripples on stream bed, *J. Hydraul. Eng.*, *123*, 58–64.

Reesink, A., and J. Bridge (2007), Influence of superimposed bedforms and flow unsteadiness on formation of cross strata in dunes and unit bars, *Sediment. Geol.*, *202*, 281–296, doi:10.1016/j.sedgeo.2007.02.005.

Reesink, A., and J. Bridge (2009), Influence of bedform superimposition and flow unsteadiness on the formation of cross strata in dunes and unit bars, part 2, further experiments, *Sediment. Geol.*, *222*, 274–300, doi:10.1016/j.sedgeo.2009.09.014.

Richards, K. J. (1980), The formation of ripples and dunes on an erodible bed, *J. Fluid Mech.*, *99*, 597–618.

Simons, D. B., and E. V. Richardson (1962), The effect of bed roughness on depth-discharge relations in alluvial channels, *Tech. Rep. Geol. Surv. Water Supply Pap., 1498-E.*, 1498–E.

Soulsby, R. L. (1997), *Dynamics of Marine Sands*, Thomas Telford Services Ltd., London.

Southard, J. B. (1971), Flume study of ripple propagation behind mounds on flat sand beds, *Sedimentology*, *16*, 251–663.

Sumer, B. M., and M. Bakioglu (1984), On the formation of ripples on an erodible bed, *J. Fluid Mech.*, *144*, 177–190.

Tjerry, S. (1995), Morphological calculation of dunes in alluvial rivers, PhD thesis, Det Naturvidenskabelige Fakultet Københavns Universitet.

Tjerry, S., and J. Fredsøe (2005), Calculation of dune morphology, *J. Geophys. Res.*, *110*, FO4013.

Todd, B. J., J. Shaw, M. Z. Li, V. E. Kostylev, and Y. Wu (2014), Distribution of subtidal sedimentary bedforms in a macrotidal setting: The Bay of Fundy, Atlantic Canada, *Cont. Shelf Res.*, *83*, 64–85, doi:10.1016/j.csr.2013.11.017.

Valance, A. (2005), Formation of ripples over a sand bed submitted to a turbulent shear flow, *Eur. Phys. J. B*, *45*, 433–442, doi:10.1140/epjb/e2005-00201-9.

Valance, A., and V. Langlois (2005), Ripple formation over a sand bed submitted to a laminar shear flow, *Eur. Phys. J. B*, *43*, 283–294, doi:10.1140/epjb/e2005-00050-6.

Van der Mark, C. F., A. Blom, and S. J. M. H. Hulscher (2008), Quantification of variability in bedform geometry, *J. Geophys. Res.*, *113*, F03020, doi:10.1029/2007JF000940.

Van Rijn, L. C. (1993), *Principles of Sediment Transport in Rivers, Estuaries and Coastal Seas*, Aqua Publications, Amsterdam.

Venditti, J. G. (2007), Turbulent flow and drag over fixed two- and three-dimensional dunes, *J. Geophys. Res.*, *112*, F04008, doi:10.1029/2006JF000650.

Venditti, J. G., M. A. Church, and S. J. Bennett (2005a), Bed form initiation from a flat sand bed, *J. Geophys. Res.*, *110*, F01009, doi:10.1029/2004JF000149.

Venditti, J. G., M. Church, S. J. Bennett (2005b), Morphodynamics of small-scale superimposed sand waves over migrating dune bed forms, *Water Resour. Res.*, *41*, W10423, doi:10.1029/2004WR003461.

Venditti, J. G., M. A. Church, and S. J. Benett (2006), On interfacial instability as a cause of transverse subcritical bedforms, *Water Resour. Res.*, *42*, W07423, doi:10.1029/2005WR004346.

Warmink, J. J., C. M. Dohmen-Janssen, J. Lansink, S. Naqshband, O. J. M. van Duin, A. J. Paarlberg, P. Termes, and S. J. M. H. Hulscher (2014), Understanding river dune splitting through flume experiments and analysis of a dune evolution model, *Earth Surf. Processes Landforms*, *39*, 1208–1220, doi:10.1002/esp.3529.

Wilcox, D. C. (1993), *Turbulence Modelling for CFD*, DCW industries Inc., La Cañada, Calif.

Yalin, M. (1985), On the determination of ripple geometry, *J. Hydraul. Eng.*, *111*, 1148–1155.

Zijlema, M. (1996), On the construction of a third-order accurate monotone convection scheme with application to turbulent flows in general domains, *Int. J. Numer. Methods Fluids*, *22*, 619–641.